

UCLA

UCLA Previously Published Works

Title

Enhanced hippocampal theta rhythmicity and emergence of eta oscillation in virtual reality

Permalink

<https://escholarship.org/uc/item/9d8942d5>

Journal

Nature Neuroscience, 24(8)

ISSN

1097-6256

Authors

Safaryan, Karen
Mehta, Mayank R

Publication Date

2021-08-01

DOI

10.1038/s41593-021-00871-z

Peer reviewed



Enhanced hippocampal theta rhythmicity and emergence of eta oscillation in virtual reality

Karen Safaryan¹✉ and Mayank R. Mehta^{1,2,3,4}✉

Hippocampal theta rhythm is a therapeutic target because of its vital role in neuroplasticity, learning and memory. Curiously, theta differs across species. Here we show that theta rhythmicity is greatly amplified when rats run in virtual reality. A novel eta rhythm emerged in the CA1 cell layer, primarily in interneurons. Thus, multisensory experience governs hippocampal rhythms. Virtual reality can be used to boost or control brain rhythms and to alter neural dynamics, wiring and plasticity.

Rats were trained to run on a 2.2-m track, either in real world (RW) or visually identical virtual reality (VR) conditions¹. Local field potential (LFP) was measured from 991 and 1,637 dorsal CA1 tetrodes of four and seven rats across 60 RW and 121 VR sessions, respectively. Consistent with previous studies¹, LFP showed 6–10-Hz theta oscillations when the rats run in either RW or VR (Fig. 1a,b, Extended Data Figs. 1–3 and Supplementary Figs. 1 and 2) that were diminished at lower speeds. However, during runs at higher speeds in VR, but not in RW, novel 2–5-Hz oscillations were also detected on several tetrodes (Fig. 1a,b, Extended Data Figs. 1–3, Supplementary Figs. 1 and 2), termed hippocampal eta oscillations. Like theta, eta was enhanced at high speeds ($>15\text{ cm s}^{-1}$) compared to low speeds (Fig. 1b).

Thus, the power spectra of the LFP from many tetrodes during runs in VR revealed a peak not only in the theta band ($\sim 7.5\text{ Hz}$) but also in the eta band ($\sim 4\text{ Hz}$) (Fig. 1b). The latter was absent during immobility. In contrast, the power spectra in RW exhibited a single peak at $\sim 8\text{ Hz}$ during run, as commonly seen^{1,2} (Fig. 1a). This is clearer in the spectrograms (Fig. 1c,d). Theta frequency is slightly reduced in VR (Fig. 1d), and there is another peak in power in the eta band during run in only VR. This is different from the type 2 theta (around 6 Hz) that appears only during periods of immobility.

The LFP spectral power could be influenced by several non-specific factors—for example, the electrode impedance, anatomical localization and behavior. Thus, we computed the LFP amplitude difference between periods of high-speed ($30\text{--}60\text{ cm s}^{-1}$) and low-speed ($5\text{--}15\text{ cm s}^{-1}$) runs in RW and VR, called amplitude index (difference divided by the sum). Remarkably, 71% (29.9%) of all tetrodes showed significantly greater eta amplitude during high-speed running epochs in VR (RW), indicating small but significant eta in the RW on some tetrodes. Indeed, eta amplitude index was 600% greater in VR than in RW (Fig. 1e and Supplementary Table 1), whereas theta amplitude index was only 100% greater (Fig. 1f). The latter is slightly different from previous reports¹, because those used a wider frequency range to compute theta, which included eta contributions. To confirm our findings, we performed a more restrictive analysis. We examined LFP power spectra separately during

run and immobility. We then computed power index, similarly to the amplitude index, as power difference during run and stop, at each frequency, and detected tetrodes with significant and prominent peaks in the eta or theta bands (Methods). This more restrictive analysis showed that 18.6% of tetrodes in VR had significantly prominent eta power index peaks compared to only 1.1% of tetrodes in RW. Similar analysis of the theta band revealed similar power index in RW and VR (84.1% and 80.4%, respectively). As a further confirmation, we restricted the analysis to the LFP data from only those tetrodes that recorded both RW and VR experiments on the same day without any intervening tetrode adjustments. This, too, showed two distinct peaks in eta and theta bands in VR but only one peak at theta in RW (Fig. 1g). These results showed significant and sustained increase in eta oscillations during run, compared to stop, in VR but not in RW. In general, rats tended to run a bit slower and had greater periods of immobility in VR than in RW (Extended Data Fig. 4), which could explain the reduction in eta power index compared to eta amplitude index. Eta might be present in the RW, even though a clear peak might not be visible in the power spectra at low frequencies, which are more vulnerable to noise and signal variability (see below). Thus, we computed the correlation between the instantaneous amplitudes of theta and eta band LFP regardless of the presence of a clear peak in the power spectrum (Fig. 1h and Extended Data Fig. 5). Most electrodes in both RW (69.93%) and VR (84.1%) showed significant correlation between theta and eta amplitudes, even when the contribution of running speed (see below) was factored out.

Why was significant and prominent eta, as defined by the strict definition of the power spectrum, often seen in only a subset of simultaneously recorded electrodes (Extended Data Fig. 6)? The anatomical depth of the electrodes in CA1 could be a key determining factor. In the RW, the lowest theta and sharp wave (SPW) amplitudes occur near the CA1 pyramidal cell layer². Both increase away from the cell layer into the dendritic region, and the SPW polarity reverses at the cell layer. Thus, SPW amplitude and polarity provide an accurate estimate of the anatomical location of an electrode with respect to the CA1 cell layer.

Hence, we measured the amplitude and polarity of SPWs during the baseline sessions preceding the tasks and compared them to the theta or eta power on the same electrodes during run in VR (Fig. 2 and Methods). The SPW amplitude was significantly correlated with the theta power for both the positive and negative polarity SPWs, such that the smallest theta occurred on tetrodes with the smallest SPW (Fig. 2a–d), similarly to RW findings³. In contrast, eta power during run was significantly anti-correlated with the SPW amplitude during immobility for both the positive and negative polarity

¹Department of Physics and Astronomy, University of California, Los Angeles, Los Angeles, CA, USA. ²W. M. Keck Center for Neurophysics, Integrative Center for Learning and Memory, and Brain Research Institute, University of California, Los Angeles, Los Angeles, CA, USA. ³Department of Electrical and Computer Engineering, University of California, Los Angeles, Los Angeles, CA, USA. ⁴Departments of Neurology and Neurobiology, University of California, Los Angeles, Los Angeles, CA, USA. ✉e-mail: safaryan@ucla.edu; mayankmehta@ucla.edu

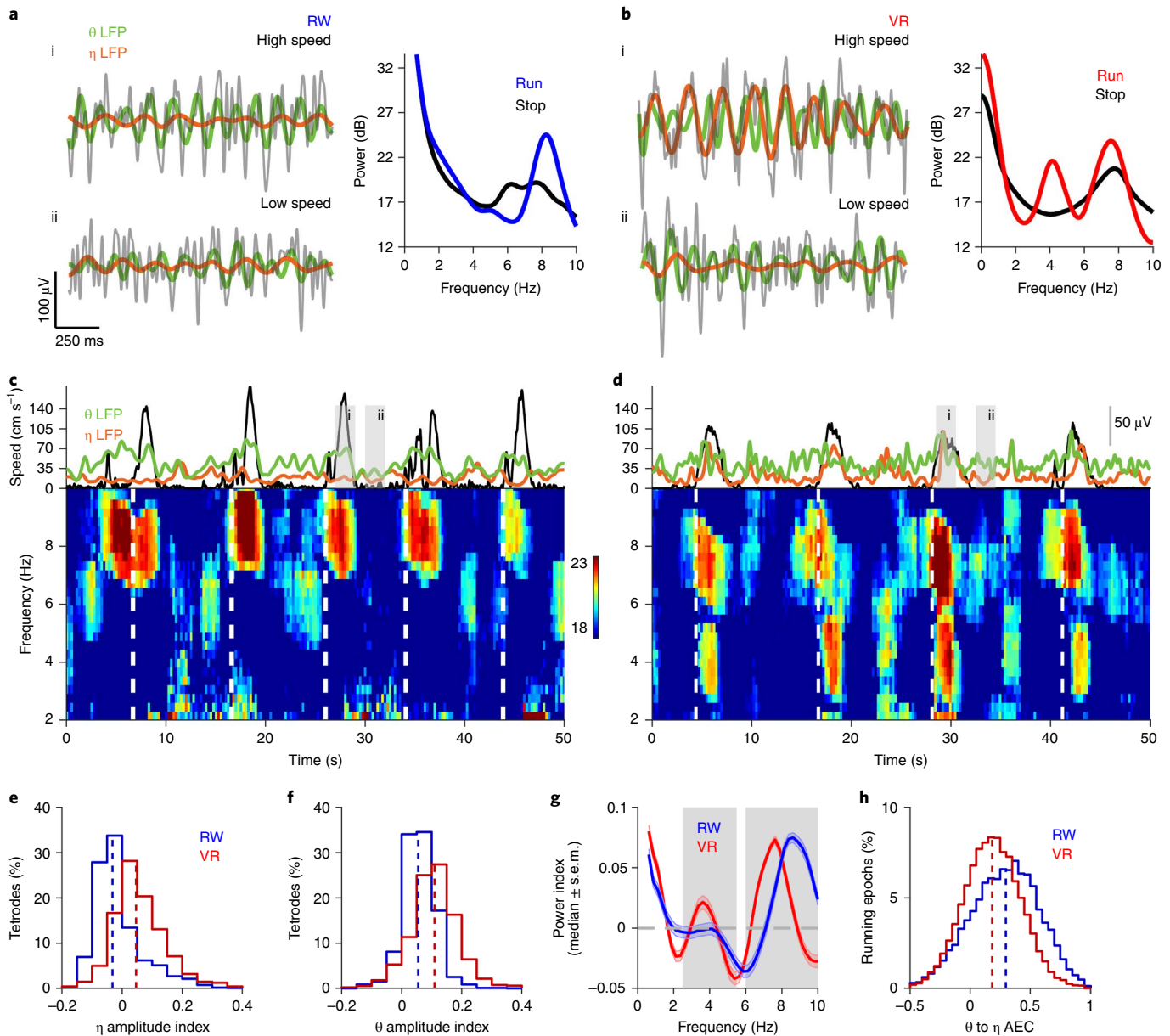


Fig. 1 | Emergence of distinct -4-Hz eta oscillation during running in VR. **a, b**, Left: the LFP, raw (gray), filtered in theta (6–10 Hz, green) and filtered in eta (2.5–5.5 Hz, brown) bands during high-speed running ($>15 \text{ cm s}^{-1}$) on track (top) and at low speeds ($<15 \text{ cm s}^{-1}$, bottom) recorded on the same tetrodes on the same day in the RW (**a**) and VR (**b**). Right: power spectra of these LFPs computed during the entire RW (blue) and VR (red) sessions at high and low speeds (including stops). **c, d**, Spectrograms (bottom, frequency versus time) of example LFPs during RW (**c**) and VR (**d**) across several run and stop epochs. Color bar denotes the power range in decibels (dB). White dashed lines indicate onset of the running epochs. The linear speed of a rat is shown above the spectrograms in black, along with the eta (brown) and theta (green) amplitude envelopes (scale bar in **d**). Highlighted in gray are periods of the LFP data shown in **a** and **b**. **e**, Distributions of the eta amplitude index (Methods) across electrodes in VR (0.063 ± 0.002 , red) was significantly greater ($P < 10^{-10}$, $\chi^2 = 540.5$, Kruskal–Wallis test) than in RW (-0.013 ± 0.003 , blue). **f**, Similar to **e** but for theta. Theta amplitude index in VR (0.115 ± 0.001 , red) was significantly greater ($P < 10^{-10}$, $\chi^2 = 414.9$, Kruskal–Wallis test) than in RW (0.056 ± 0.002 , blue). **g**, Population-averaged power index (between run and stop; Methods) for tetrodes recorded on the same day in RW and VR ($n = 150$, obtained from four rats and 39 sessions) that showed significant and sustained eta in RW or VR. **h**, Distributions of amplitude envelope correlations (AECs) computed as partial correlation (running speed as a controlling variable) between the LFP eta and theta amplitude envelopes across running epochs in RW (0.28 ± 0.0019) were significantly greater ($P < 10^{-10}$, $\chi^2 = 1864.8$, Kruskal–Wallis test) than in VR (0.18 ± 0.0013). Shades in **g** show s.e.m. θ , theta; η , eta.

SPWs, with the highest eta power coinciding with the lowest SPW amplitude (Fig. 2a,b,c,e).

This ensemble analysis could be influenced by differences in behavior across sessions. Therefore, we computed the correlation between the SPW amplitude and theta or eta power across only those electrodes that were recorded simultaneously within a ses-

sion. As expected, the SPW and theta amplitudes were significantly positively correlated for most sessions (Fig. 2f). But the correlation was significantly negative between SPW and eta amplitude (Fig. 2f). Thus, whereas theta magnitude is smallest in the CA1 cell layer and larger in the dendrites, eta amplitude shows the opposite pattern, with highest amplitude near the CA1 cell layer in VR.

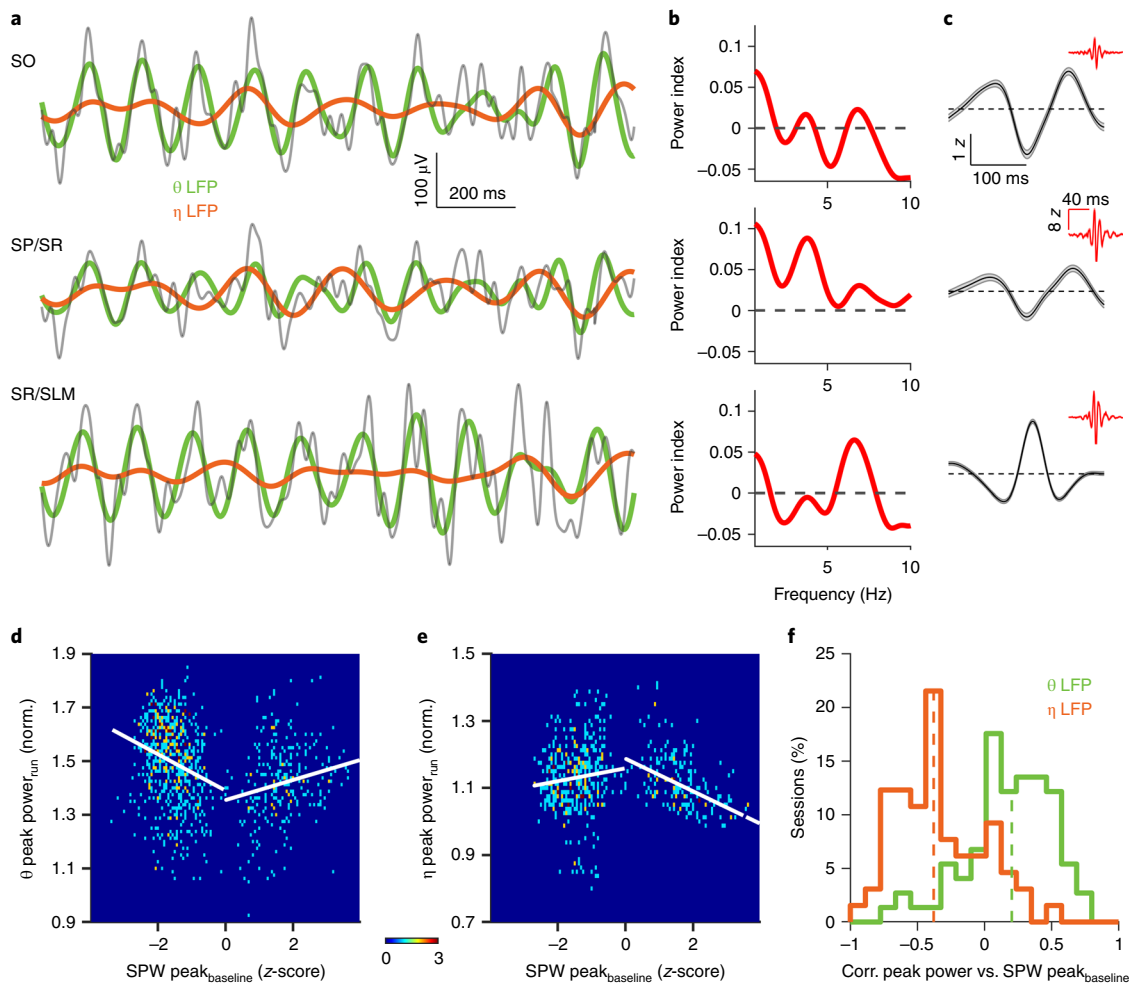


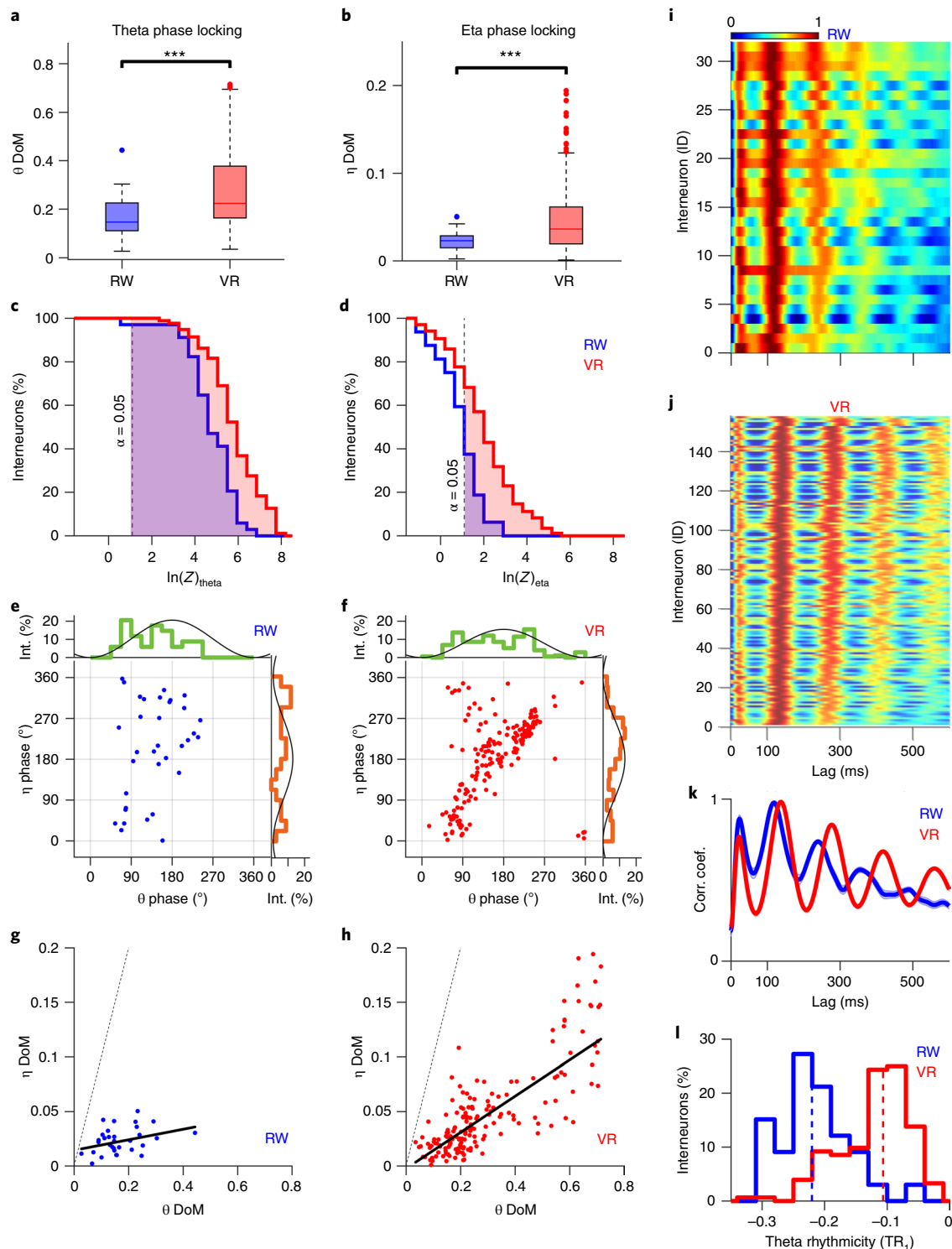
Fig. 2 | Theta is weakest and eta is strongest in the CA1 cell layer. **a**, LFP from three simultaneously recorded tetrodes (same color scheme as Fig. 1a) in a VR session during high-speed (>30 cm s $^{-1}$) run. **b**, LFP power index (same as in Fig. 1f) for these electrodes (red). **c**, Average z-scored (mean \pm s.e.m.) ripple traces (red, centered at the peak of the ripple powers) and associated SPWs (black) for the corresponding electrodes computed during the baseline session preceding the task. The eta band signal (brown) is the highest in the middle row, which has the smallest SPW amplitude, whereas the theta band signal (green) shows the opposite pattern. SO (stratum oriens), SP (stratum pyramidale), SR (stratum radiatum) and SLM (stratum lacunosum moleculare) indicate the presumed depth of the electrodes based on SPW properties. **d**, Density plot of the z-scored SPW peak amplitude and polarity during rest versus normalized (norm.) theta power during run in VR. Theta and SPW amplitudes were significantly correlated for both the positive polarity SPW ($n = 361$, $r = 0.24$, $P < 10^{-5}$; Spearman's rank correlation, here and subsequently, unless specified otherwise) and the negative polarity SPW ($n = 737$, $r = -0.24$, $P < 10^{-10}$). **e**, Similar to **d** but for the eta power, which shows the opposite to theta pattern (for positive SPW, $n = 279$, $r = -0.53$ and $P < 10^{-10}$; for negative SPW, $n = 472$, $r = 0.11$ and $P = 0.04$). **f**, Distributions of correlation (corr.) values between the absolute value of z-scored SPW peak amplitude during rest and eta normalized power during run were significantly negative (-0.34 ± 0.04 , $P < 10^{-10}$, $n = 70$), but the same for theta were significantly positive (0.20 ± 0.03 , $P < 10^{-5}$, $n = 85$). Only the sessions with at least four electrodes in the hippocampus were used. Shades in **c** show s.e.m. θ , theta; η , eta.

Eta was distinct from the type 2 theta that appears during immobility for several reasons. Similarly to type 1 theta, whose amplitude increases with running speed, eta amplitude also increased with running speed. Furthermore, the seed dependence of theta and eta amplitude was non-monotonic in VR, and speed dependence of theta frequency differed between VR and RW (Extended Data Fig. 3).

Hippocampal theta is influenced by the medial septal inputs^{4,5}, which target hippocampal inhibitory neurons. Thus, we examined the rhythmicity of 34 and 174 putative inhibitory interneurons in RW and VR, respectively. The number of interneurons in VR is far greater than in RW, which is not the case for pyramidal neurons, because of previously reported large shutdown of CA1 pyramidal cells in VR¹. The magnitudes of both theta (Fig. 3a) and eta (Fig. 3b) phase locking of the interneurons were nearly twice as large in VR

than RW. All interneurons showed significant theta phase locking in both RW and VR (Fig. 3c). But, significantly, eta phase-locked interneurons in VR (66.6%) were far greater than in RW (35.3%) (Fig. 3d). The interneurons' preferred theta phase was similar in both worlds (Fig. 3e,f). However, the population of interneurons, and not pyramidal neurons (Supplementary Fig. 3), showed greater eta phase preference in VR by preferentially firing near the eta peak (Fig. 3e,f). As a result, despite a wide range of the preferred theta and eta phases, far greater (circular) correlation was seen between eta and theta phase preferences of interneurons in VR (Fig. 3f) than in RW (Fig. 3e). Similarly, eta to theta co-modulation of interneurons was stronger in VR (Fig. 3h) than in RW (Fig. 3g).

Finally, the auto-correlations of the interneurons showed greater theta rhythmicity in VR than in RW (Fig. 3i-k), evidenced by larger amplitudes of second, third and fourth peaks (Fig. 3i and Extended



Data Figs. 7 and 8). This suggests that increased theta rhythmicity of interneurons might be related to the emergence of eta rhythm in VR. Indeed, interneurons with higher theta rhythmicity showed greater theta and eta phase locking in VR (Extended Data Fig. 9) but not in RW. CA1 pyramidal neurons also showed enhanced theta rhythmicity in VR (Supplementary Figs. 4–6). However, unlike the interneurons, CA1 pyramidal neurons showed very little eta modulation in both RW and VR.

These results reveal the crucial role of multisensory inputs in hippocampal rhythmogenesis. We found that the dorsal hippocampal CA1 of rodents can simultaneously exhibit two distinct

slow oscillations, eta and theta, while running in the RW, and both are substantially enhanced while running in a visually similar VR (Supplementary Fig. 7). Notably, a third of electrodes showed significant eta modulation in the RW, and this fraction doubled in VR.

Whereas theta was strongest on dendrite-rich regions of CA1, eta was weaker in those areas and strongest in the CA1 cell layer. This suggests that eta might arise locally within CA1, whereas theta might come from other sources, such as medial septum. Consistently, a third of CA1 interneurons showed significant eta modulation in the RW, and this fraction doubled in VR, reflecting similar changes in the LFP. In fact, the eta and theta amplitudes

Fig. 3 | Enhanced TR and eta and theta modulation of interneurons in VR. **a**, Magnitude of the theta phase locking of interneurons in VR (0.29 ± 0.014 , $n=174$ from seven rats) is significantly greater than in RW (0.16 ± 0.014 , $n=34$ from four rats) ($\chi^2=16.35$, $P<0.001$, Kruskal-Wallis test) by 81%. Boxes show the 25th and 75th percentiles in the RW and VR groups; the central line shows the median; the whiskers show data in the 1.5x interquartile range outside of the 25th to 75th percentiles. **b**, Same as **a** but for eta, showing significantly greater (150%) phase locking of interneurons in VR (0.05 ± 0.003) compared to RW (0.02 ± 0.001) ($\chi^2=14.25$, $P<0.001$, Kruskal-Wallis test). **c**, Cumulative distribution of the log-transformed Rayleigh's Z of theta modulation for interneurons shows significantly modulated (shaded area) cells in VR ($n=174$, 100%) and in RW ($n=33$, 97.05%) at $P<0.05$ (dashed line). **d**, Same as **c** but for eta band, showing that 31.37% more cells are significantly modulated in VR ($n=116$, 66.66%) than in RW ($n=12$, 35.29%). **e**, Relationship between preferred theta and eta phases of interneurons in RW ($n=34$, $r=-0.44$, $P=0.011$; circ-circ corr., circular statistics; Rayleigh statistics). The corresponding distributions (circ. (mean \pm s.d.)) of preferred theta ($137.82 \pm 1.32^\circ$, MVL = 0.48, green) and eta ($291.67 \pm 1.39^\circ$, MVL = 0.21, brown) phases are specified. A reference theta/eta cycle is plotted in black (LFP positive polarity is downward). **f**, Same as in **e** but for VR ($n=174$, $r=0.35$, $P=1.8 \times 10^{-6}$). The corresponding distributions of preferred theta ($155.4 \pm 1.38^\circ$, MVL = 0.42, green) and eta ($219.41 \pm 1.35^\circ$, MVL = 0.29, brown) phases in VR are shown. The distributions are significantly different for theta ($P=0.02$, $V=0.132$, Kuiper's test) and eta ($P=0.05$, $V=0.339$, Kuiper's test) preferred phases between RW and VR. **g**, No significant correlation between eta and theta DoMs of interneurons was seen in RW ($n=34$, $r=0.28$, $P=0.11$, partial correlation factoring out number of spikes). **h**, Same as **g** but in VR, showing strong positive correlation ($n=174$, $r=0.75$, $P<10^{-10}$, partial correlation factoring out number of spikes). **i**, Corrected auto-correlations ordered according to the increasing TR₁ values for RW. The auto-correlograms are normalized by their first theta peak values as for the place cells. **j**, Same as **i** but for VR, showing more theta peaks—that is, greater rhythmicity—than in RW. **k**, Population average of auto-correlations show greater theta rhythmicity (TR) in VR compared to RW. **l**, Histograms of the TR₁ distributions in VR (-0.118 ± 0.004) are 82% greater ($P<10^{-10}$, $\chi^2=47.31$, Kruskal-Wallis test) than in RW (-0.215 ± 0.009). θ , theta; η , eta; MVL, mean vector length.

were highly correlated for most electrodes in both VR and RW during run and not during immobility. In contrast, very few place cells, which have more extensive dendrites, showed eta modulation, but most showed strong theta modulation in both RW and VR. The rodent eta rhythm in VR might be related to the irregular bouts of 1–5-Hz oscillations reported in humans and non-human primates while they are immobile and performing tasks in VR^{6–9}. On the other hand, eta amplitude in our studies was greater during locomotion than immobility. When humans walk, a higher, ~8-Hz theta oscillation appears in some hippocampal LFPs, which is either absent or substantially reduced in VR^{6,10}.

One possible reason for these differences could be that humans were immobile in these VR studies and could make only restricted eye and hand movements, whereas rats in our studies ran similarly in RW and VR, making the full sets of running movements. However, because of the body-fixed condition in VR, the linear acceleration is minimized. Thus, we hypothesize that running movements of the body, without significant linear acceleration, are sufficient to enhance eta and theta rhythms (Supplementary Fig. 8). We hypothesize that the presence of linear acceleration in RW makes theta frequency dependent on speed or acceleration^{2,5}, thereby reducing the overall theta rhythmicity. The enhanced theta rhythmicity in VR, when coupled with low-frequency signals, especially via phase–phase coupling, could generate stronger eta rhythm in VR. Acceleration dependence of theta frequency in RW would, therefore, reduce not only theta rhythmicity but also eta rhythm. This was further supported by our findings that eta–theta phase–phase coupling was much greater in VR than RW, but the eta–theta amplitude coherence was comparably large in both worlds. This can explain why a clear power spectral peak in eta band was seen only in VR, but increased eta band power during run was also seen in a third of electrodes in the RW. Other studies reported theta skipping in excitatory neurons in certain tasks¹¹. This is probably different than our findings because we did not see a major difference in the eta modulation of pyramidal neurons, and we saw eta rhythm at the level of field potential. Analysis of eta–theta coherence in these tasks (Supplementary Fig. 9) and investigation of interneurons, similar to our RW data, could be useful. The eta rhythm is unlikely to be related to the respiration-related rhythm¹², because it is weaker in the cell layer and stronger below the cell layer, unlike eta rhythm. Eta is not a volume-conducted signal from other brain areas because it is highest in the CA1 cell layer and lower above and below.

It is plausible that eta is generated within the CA1 cell layer by a local network of excitatory–inhibitory neurons. CA1 slices show eta band signals. Accordingly, it is not the activity of pyramidal neurons

but the activity of inhibitory interneurons that was differentially modulated by eta in VR compared to RW. This is further supported by several studies demonstrating the role of CA1 interneurons in hippocampal slow oscillations¹³. The reduced theta frequency in VR could arise due to a slowdown of the CA1 excitatory–inhibitory network due to the shutdown of a large number of pyramidal neurons¹. Coupled with theta, eta can enhance the rhythmicity and alter the speed dependence of the theta rhythm in VR. This mechanism can be most prominent at the large dendritic branches of the pyramidal cells, where theta is largest. Recent theories suggest that memories are encoded on segments of dendritic branches in pyramidal neurons flanked by inhibitory synapses^{14,15}. This would result in decoupling of the dendritic activity from the soma, as observed recently¹⁶.

The eta oscillations, nearly half as slow as theta oscillations, could segregate activity of hippocampal neural populations into parallel streams of information processing throughout theta cycles^{11,17}. Eta can enhance cortico-hippocampus interaction, because the 4-Hz rhythm is frequent in the neocortex¹⁸. Eta rhythm and enhanced theta rhythmicity in VR would influence neural synchrony and via N-methyl-D-aspartate receptor-dependent synaptic plasticity, which crucially depends on the neural rhythmicity^{19,20} in dendritic branch-specific fashion to alter hippocampal circuit and learning^{14–16}. Impaired hippocampal slow oscillations have been implicated in several cognitive impairments. VR could, thus, be used to enhance hippocampal slow oscillations and neuroplasticity to treat learning and memory impairments.

Online content

Any methods, additional references, Nature Research reporting summaries, source data, extended data, supplementary information, acknowledgements, peer review information; details of author contributions and competing interests; and statements of data and code availability are available at <https://doi.org/10.1038/s41593-021-00871-z>.

Received: 18 December 2020; Accepted: 7 May 2021;
Published online: 28 June 2021

References

- Ravassard, P. et al. Multisensory control of hippocampal spatiotemporal selectivity. *Science* **340**, 1342–1346 (2013).
- Kropff, E., Carmichael, J. E., Moser, E. I. & Moser, M. B. Frequency of theta rhythm is controlled by acceleration, but not speed, in running rats. *Neuron* **109**, 1029–1039 (2021).
- Buzsáki, G. Hippocampal sharp waves: their origin and significance. *Brain Res.* **398**, 242–252 (1986).

4. Winson, J. Loss of hippocampal theta rhythm results in spatial memory deficit in the rat. *Science* **201**, 160–163 (1978).
5. Fuhrmann, F. et al. Locomotion, theta oscillations, and the speed-correlated firing of hippocampal neurons are controlled by a medial septal glutamatergic circuit. *Neuron* **86**, 1253–1264 (2015).
6. Bohbot, V. D., Copara, M. S., Gotman, J. & Ekstrom, A. D. Low-frequency theta oscillations in the human hippocampus during real-world and virtual navigation. *Nat. Commun.* **8**, 14415 (2017).
7. Ekstrom, A. D. et al. Human hippocampal theta activity during virtual navigation. *Hippocampus* **15**, 881 (2005).
8. Jutras, M. J., Fries, P. & Buffalo, E. A. Oscillatory activity in the monkey hippocampus during visual exploration and memory formation. *Proc. Natl Acad. Sci. USA* **110**, 13144–13149 (2013).
9. Goyal, A. et al. Functionally distinct high and low theta oscillations in the human hippocampus. *Nat. Commun.* **11**, 2469 (2020).
10. Aghajan, Z. M. et al. Theta oscillations in the human medial temporal lobe during real-world ambulatory movement. *Curr. Biol.* **27**, 3743–3751 (2017).
11. Brandon, M. P., Bogaard, A. R., Schultheiss, N. W. & Hasselmo, M. E. Segregation of cortical head direction cell assemblies on alternating θ cycles. *Nat. Neurosci.* **16**, 739–748 (2013).
12. Yanovsky, Y., Ciatipis, M., Draguhn, A., Tort, A. B. & Brankač, J. Slow oscillations in the mouse hippocampus entrained by nasal respiration. *J. Neurosci.* **34**, 5949–5964 (2014).
13. Jackson, J. et al. Reversal of theta rhythm flow through intact hippocampal circuits. *Nat. Neurosci.* **17**, 1362–1370 (2014).
14. Mehta, M. R. Cooperative LTP can map memory sequences on dendritic branches. *Trends Neurosci.* **27**, 69–72 (2004).
15. Mehta, M. R. From synaptic plasticity to spatial maps and sequence learning. *Hippocampus* **25**, 756–762 (2015).
16. Moore, J. J. et al. Dynamics of cortical dendritic membrane potential and spikes in freely behaving rats. *Science* **355**, eaaj1497 (2017).
17. Deshmukh, S. S., Yoganarasimha, D., Voicu, H. & Knierim, J. J. Theta modulation in the medial and the lateral entorhinal cortices. *J. Neurophysiol.* **104**, 994–1006 (2010).
18. Karalis, N. et al. 4-Hz oscillations synchronize prefrontal-amygdala circuits during fear behavior. *Nat. Neurosci.* **19**, 605–612 (2016).
19. Kumar, A. & Mehta, M. R. Frequency-dependent changes in NMDAR-dependent synaptic plasticity. *Front. Comput. Neurosci.* **5**, 38 (2011).
20. Narayanan, R. & Johnston, D. Long-term potentiation in rat hippocampal neurons is accompanied by spatially widespread changes in intrinsic oscillatory dynamics and excitability. *Neuron* **56**, 1061–1075 (2007).

Publisher's note Springer Nature remains neutral with regard to jurisdictional claims in published maps and institutional affiliations.

© The Author(s), under exclusive licence to Springer Nature America, Inc. 2021

Methods

Subjects and surgery. Detailed methods were described previously¹. Briefly, seven adult male Long-Evans rats (approximately 3.5 months old at the start of training) were implanted with 25–30-g custom-built hyperdrives containing up to 22 independently adjustable tetrodes (13- μ m nichrome wires) positioned over both dorsal CA1 areas (–4.0 mm anteroposterior and 2.4 mm medial lateral relative to bregma). Surgery was performed under isoflurane. Analgesia was achieved by using lidocaine (0.5 mg kg⁻¹, subcutaneous) and buprenorphine (0.03 mg kg⁻¹, intraperitoneal). Dura mater was removed, and the hyperdrive was lowered until the cannulae were 100 μ m above the surface of the neocortex. The implant was anchored to the skull with 7–9 skull screws and dental cement. The occipital skull screw was used as ground for electrophysiology. Electrodes were adjusted each day until stable single units were obtained. Positioning of electrodes in the CA1 was confirmed through the presence of SPW ripples during immobility.

VR and RW tasks. The virtual environment consisted of a 220 \times 10-cm linear track floating 1 m above the virtual floor and centered in a 3 \times 3 \times 3-m room^{1,21}. Alternating 5-cm-wide green and blue stripes on the surface of the track provided optic flow. A 30 \times 30-cm white grid on the black floor provided parallax-based depth perception. Distinct distal visual cues covered all four walls and provided the only spatially informative stimuli in the VR. In RW, rats ran back and forth on a 220 \times 6-cm linear track that was placed 80 cm above the floor. The track was surrounded by four 3 \times 3-m curtains that extended from floor to ceiling. The same stimuli on the walls in the virtual room were printed on the curtains; thus, the distal visual cues were similar in RW and VR.

Data acquisition, LFP processing, spike detection, sorting and cell classification. Spike and LFP data were collected by 22 independently adjustable tetrodes. Signals from each tetrode were digitized at 32 kHz and wide-band pass-filtered between 0.1 Hz and 9 kHz (Digital Lynx SX, Neuralynx). This was downsampled to 1.25 kHz to obtain the LFPs or filtered between 600 and 6,000 Hz for spike detection. LFP positive polarity was downward¹. Unless otherwise stated, the band-pass LFP filtering was done by using a zero-lag fourth-order Butterworth filter. Spikes were detected offline using a non-linear energy operator threshold¹. After detection, spike waveforms were extracted, upsampled four-fold using cubic spline, aligned to their peaks and downsampled back to 32 data points. PyClust software (a modified version of <http://redishlab.neuroscience.umn.edu/mclust/MClust.html>) was used to perform spike sorting²². Units were then classified into putative pyramidal neurons and interneurons based on spike waveforms, complex spike index and rates¹.

Offline analyses were performed using custom code written in MATLAB (MathWorks).

Analysis of LFP and spike data during behavior. Running epochs were defined as continuous periods of running (>10 cm s⁻¹) for 2 s or more. Immobility was defined as periods of low speed (<2.5 cm s⁻¹) for 2 s or more. Thus, the low-speed range, which excludes periods of immobility, was taken as a range from 5 to 15 cm s⁻¹. In addition, correlation coefficients of the amplitudes of the different frequency bands with speeds were computed below and above 10 cm s⁻¹ to capture dynamics during transition periods from rest to run and running epochs.

Spectral analysis of oscillatory activity was computed using a multi-taper method^{23,24} by Chronux toolbox (<http://chronux.org>). A window size of 4 s (average running time during the task) and 3–5 tapers were used with a 75% overlap over frequencies ranging from 0.5 to 30 Hz. The spectral power was computed separately during running epochs and immobility states. The power spectral index was computed as the difference of power between running epochs and immobility at each frequency over their sum (Figs. 1h and 2b and Extended Data Figs. 1 and 2). Significance of the power difference between running epochs and immobility in the theta and eta bands was determined using the Kruskal–Wallis non-parametric test ($\alpha = 0.01$). To reduce non-specific effects, the power spectra of each tetrode were normalized by average power in 0.5–30-Hz range on that tetrode separately for the running epochs and immobility states. Theta and eta power peaks were detected using peak prominence of 0.01 or more within the respective frequency bands (findpeaks.m from the signal toolbox in MATLAB). The prominence was defined as the height of the peaks at the levels of highest troughs (MathWorks). With few exceptions, this led to the detection of eta peaks predominantly during running epochs in VR. The prominence of eta index peaks greater than the 5th percentile of the theta index peaks was considered as significant. Peak power was computed as an average power within 1 Hz at the detected peak.

This power spectrum-based method requires comparatively long periods of unitary behavior (for example, run or stop) over which the power spectra are computed. To obtain an estimate of the instantaneous values of eta and theta bands, we filtered the LFP data in either eta ranges (2.5–5.5 Hz) or theta ranges (6–10 Hz) and computed its Hilbert transform. Amplitude difference index was computed as the difference of the mean amplitude in theta (or eta) band during high-speed (30–60 cm s⁻¹) and low-speed (5–15 cm s⁻¹) runs, divided by their sum (Fig. 1c,d). Significance level of theta (or eta) modulation of LFP was determined by comparing the distributions of the LFP amplitude in theta (or eta) band during high-speed (30–60 cm s⁻¹) versus low-speed (5–15 cm s⁻¹) runs and using the

non-parametric Kruskal–Wallis test. In addition, alternative, non-parametric estimates were performed by computing robust regression fits between amplitude envelope and speed.

Theta frequency was computed using three methods: cycle detection using Hilbert-transformed phase jumps, the derivative of Hilbert transform phase and the short-time Fourier transform. The cycle method results are reported (Extended Data Fig. 3).

SPW and ripple detection. To estimate the electrode depth, we performed SPW ripple analysis during periods of immobility in baseline sessions preceding the tasks. LFP data were filtered in ripple (80–250 Hz) band. This signal was z -scored by subtracting the mean value and dividing by the standard deviation of the ripple band LFP to obtain the z -scored ripple band signal. The double-threshold crossing method was applied to the LFP z -scores^{25,26} to detect ripple events. All time points with larger than a first threshold ($z > 3$) were identified as part of a ripple event. Only events with a peak value larger than a second threshold ($z > 10$) and duration longer than 30 ms were retained (Fig. 2c). Ripple events separated by less than 50 ms were stitched together. To detect the concomitant SPW, LFPs were filtered in the 6–25-Hz range. These signals were z -scored and amplitude detected at the times of each associated ripple peak. These SPWs were averaged across all the ripples in a session to obtain the average SPW (Fig. 2c).

Place field detection. A unit was considered track (goal) active if its mean firing rate on track (goal) was at least 1 Hz. Opposite directions of the track were treated as independent and linearized. A place field was defined as a region where the firing rate exceeded 5 Hz for at least 5 cm. The boundaries of a place field were defined as the point where the firing rate first drops below 5% of the peak rate (within the place field) for at least 5 cm and exhibits significant activity on at least five trials¹.

Phase locking detection and characterization. Instantaneous amplitudes and phases were estimated by Hilbert transform of the filtered signals as below:

$$LFP(t) = \rho(t) e^{-i\varphi(t)}$$

where $\rho(t)$ is instantaneous amplitude and $\varphi(t)$ is instantaneous phase.

The Rayleigh circular uniformity test was computed to test significance of phase locking. The first circular moment was given as $m_1 = \left(\frac{1}{n}\right) \sum_{j=1}^n e^{i\varphi_j} = R e^{i\mu}$,

where φ_j are phases of n spikes. The preferred LFP phase of spikes is, thus, given by μ , and the magnitude of phase locking was given by R . The magnitude of phase locking was defined as depth of modulation (DoM)²⁷. The Rayleigh statistics $Z = R^2 n$ ($n > 50$, only neurons with at least 50 spikes were used) and the probability of the null hypothesis of sample uniformity ($P = e^{-Z}$) were applied^{28,29}.

Spike auto-correlogram, Gaussian mixture model fit and theta rhythmicity index calculation. Spike-time auto-correlograms were computed using accuracy of 1 ms, smoothed by 20-ms Gaussian function and normalized by the number of spikes to obtain probability at lags. Auto-correlograms $Y(t)$ were fit using the following Gaussian mixture model^{11,30,31}:

$$Y(t) = \left[\left(a \times e^{-\frac{t}{\tau_1}} \right) \sum_{n=1}^N \left(\frac{1}{\sqrt{2\pi}\sigma} e^{-\frac{(t-n\omega)^2}{2\sigma^2}} \right) + b \right] e^{-\frac{t}{\tau_2}}$$

where t is the auto-correlation lag time (ranging from 60 to 600 ms) and a , τ_1 , ω , σ , b and τ_2 are the fit parameters. The Gaussian terms are used to fit theta peak and its harmonics (ω is a first theta lag). τ_1 and τ_2 are the exponential decay constants for the magnitude of rhythmicity and overall auto-correlogram falloff rate due to finite amount of data, respectively. a is the rhythmicity factor, and b is constant background or non-rhythmic component. Five Gaussian ($n = 5$) were used to fit the auto-correlogram. The amplitude of the first Gaussian ($n = 1$) provides an estimate of theta modulation while removing non-specific effects arising from the duration of the place field and the duration of recording. Theta rhythmicity (TR) was defined as $TR(n) = (\text{amplitude}(n+1) - \text{amplitude}(n)) / \max(\text{amplitude}(n), \text{amplitude}(n+1))$ where n is an auto-correlogram peak index at theta or its harmonics and varies from 1 to 3. Theta skipping^{11,17} was defined as TR with $n = 1$.

Statistics. Unless otherwise stated, statistical significance between two distributions of linear variables was evaluated using the non-parametric Kruskal–Wallis test. Tests for populations significantly different from zero were also performed using the non-parametric Kruskal–Wallis test. Average values are reported in the form mean \pm s.e.m. unless otherwise stated. Median values of histograms are depicted as a dashed line in all main figures. Circular statistics were computed using the CircStat toolbox. Binomial confidence interval was computed using the Clopper–Pearson method from the statistics toolbox in MATLAB (binofit.m). Data distributions were assumed to be normal, but this was not formally tested. To reduce the contribution of outliers, unless otherwise stated, we used non-parametric Spearman's rank correlation to compute all correlation coefficients, including partial correlations. No statistical methods were used to

predetermine sample size in these exploratory studies, but our sample sizes are similar to those reported in previous publications^{1,11,13,21}. Neural and behavioral data analyses were conducted in an identical way regardless of the identity of the experimental condition from which the data were collected, with the investigator blinded to group allocation during data collection and/or analysis. Hippocampal units were isolated and clustered blindly by three different lab members. The experiments were conducted by three different lab members. Similar sessions in RW and VR were run over all rats, which were selected randomly. Covariates were controlled across sessions and within rats. No rat was excluded. The presence of the SPW ripples was used to identify hippocampal tetrodes. In addition, classified putative pyramidal cells were used to verify selection. Both methods were widely used to verify hippocampal tetrodes. See also the corresponding Life Sciences Reporting Summary.

Reporting Summary. Further information on research design is available in the Nature Research Reporting Summary linked to this article.

Data availability

The data that support the findings of this study are available from the corresponding author upon reasonable request.

Code availability

The software used for data acquisition and analysis are available using the web links provided in the Methods. PyClust is a modified version of <http://redishlab.neuroscience.umn.edu/mclust/MClust.html>.

References

21. Cushman, J. D. et al. Multisensory control of multimodal behavior: do the legs know what the tongue is doing? *PLoS ONE* **8**, e80465 (2013).
22. Willers, B. Multimodal sensory contributions to hippocampal spatiotemporal selectivity. <https://escholarship.org/uc/item/94s3s84c> (Doctoral dissertation, University of California, Los Angeles, 2013).
23. Mitra, P. P. & Pesaran, B. Analysis of dynamic brain imaging data. *Biophys. J.* **76**, 691–708 (1999).
24. Bokil, H., Andrews, P., Kulkarni, J. E., Mehta, S. & Mitra, P. P. Chronux: a platform for analyzing neural signals. *J. Neurosci. Methods* **192**, 146–151 (2010).
25. Ego-Stengel, V. & Wilson, M. A. Disruption of ripple-associated hippocampal activity during rest impairs spatial learning in the rat. *Hippocampus* **20**, 1–10 (2010).
26. Ji, D. & Wilson, M. A. Coordinated memory replay in the visual cortex and hippocampus during sleep. *Nat. Neurosci.* **10**, 100 (2007).
27. Skaggs, W. E., McNaughton, B. L., Wilson, M. A. & Barnes, C. A. Theta phase precession in hippocampal neuronal populations and the compression of temporal sequences. *Hippocampus* **6**, 149–172 (1996).
28. Sirota, A. et al. Entrainment of neocortical neurons and gamma oscillations by hippocampal theta rhythm. *Neuron* **60**, 683–697 (2008).
29. Siapas, A. G., Lubenov, E. V. & Wilson, M. A. Prefrontal phase locking to hippocampal theta oscillations. *Neuron* **46**, 141–151 (2005).
30. Royer, S., Sirota, A., Patel, J. & Buzsáki, G. Distinct representations and theta dynamics in dorsal and ventral hippocampus. *J. Neurosci.* **30**, 1777–1787 (2010).
31. Climer, J. R., DiTullio, R., Newman, E. L., Hasselmo, M. E. & Eden, U. T. Examination of rhythmicity of extracellularly recorded neurons in the entorhinal cortex. *Hippocampus* **25**, 460–473 (2015).

Acknowledgements

We thank P. Ravassard, A. Kees, L. Acharya and A. Hachisuka for providing the experimental data; Z. Aghajan and B. Willers for help with the analyses; and S. Dhingra, K. Choudhary and current and former Mehta lab members for discussions, careful reading of the manuscript and valuable comments. This study was funded by the W. M. Keck Foundation, an AT&T research grant, National Science Foundation grant no. 1550678 and National Institutes of Health grant no. 1U01MH115746, all to M.R.M. The findings were presented at Society for Neuroscience meetings (abstract nos. 263.02 (2016), 523.08 (2017), 508.07 (2018) and 083.03 (2019)).

Author contributions

K.S. and M.R.M. designed the study. M.R.M. advised on all aspects of the analysis and experiments. K.S. analyzed the data and generated the figures. K.S. and M.R.M. wrote the paper.

Competing interests

The authors declare no competing interests.

Additional information

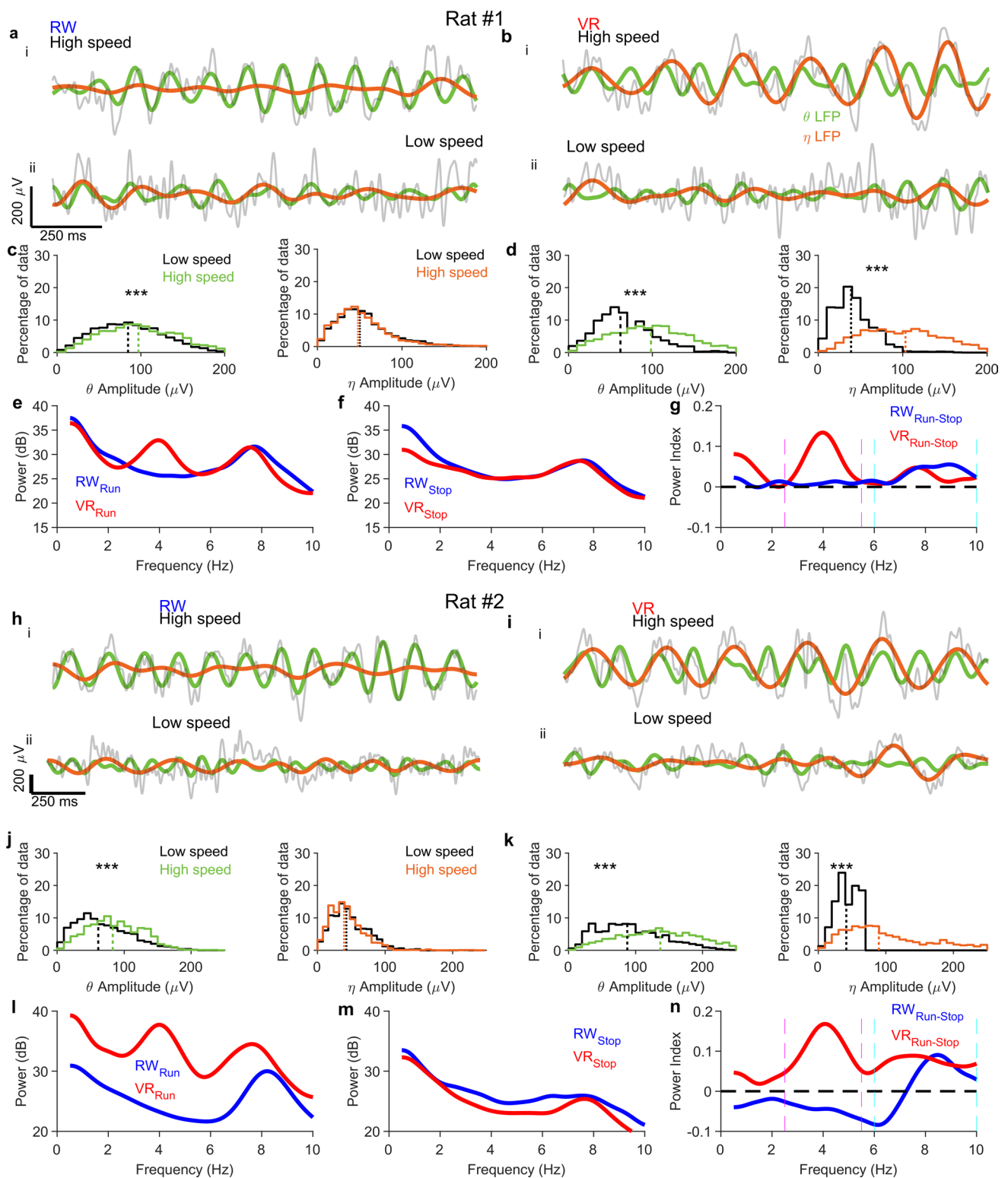
Extended data is available for this paper at <https://doi.org/10.1038/s41593-021-00871-z>.

Supplementary information The online version contains supplementary material available at <https://doi.org/10.1038/s41593-021-00871-z>.

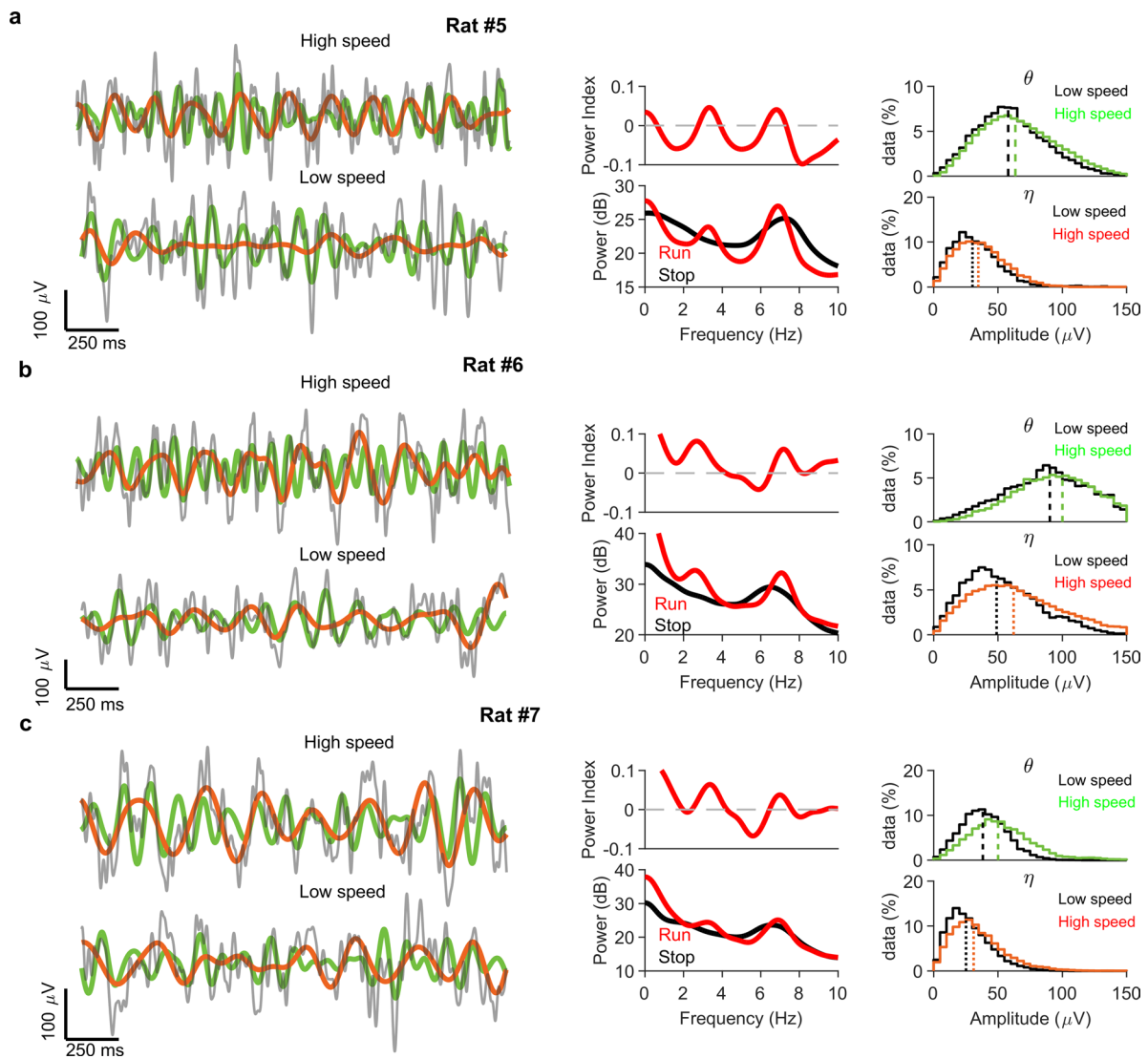
Correspondence and requests for materials should be addressed to K.S. or M.R.M.

Peer review information *Nature Neuroscience* thanks the anonymous reviewers for their contribution to the peer review of this work.

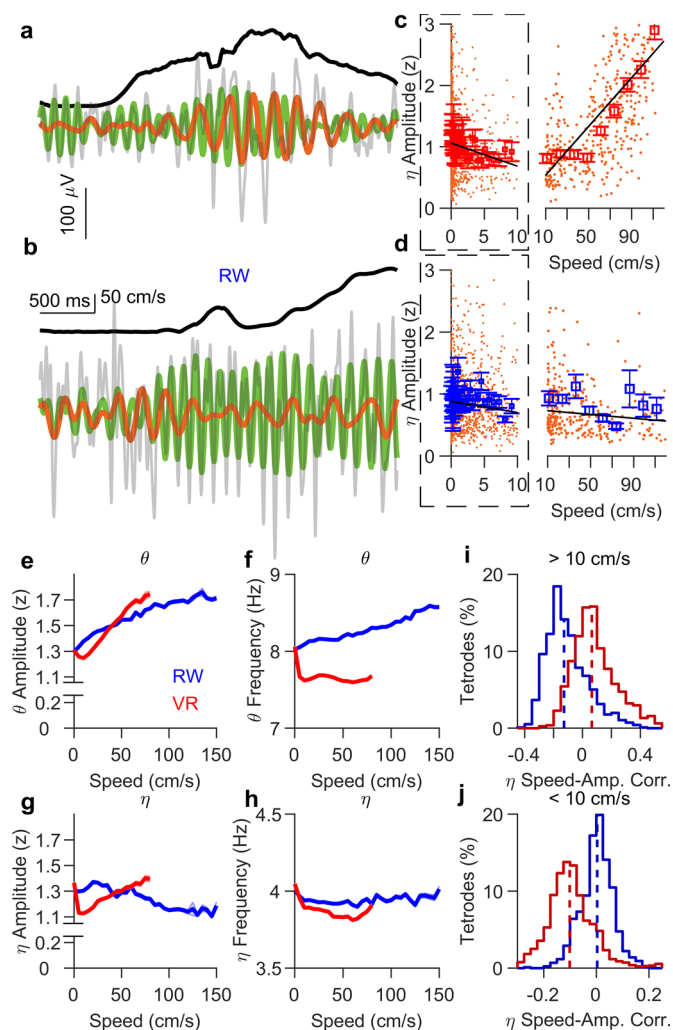
Reprints and permissions information is available at www.nature.com/reprints.



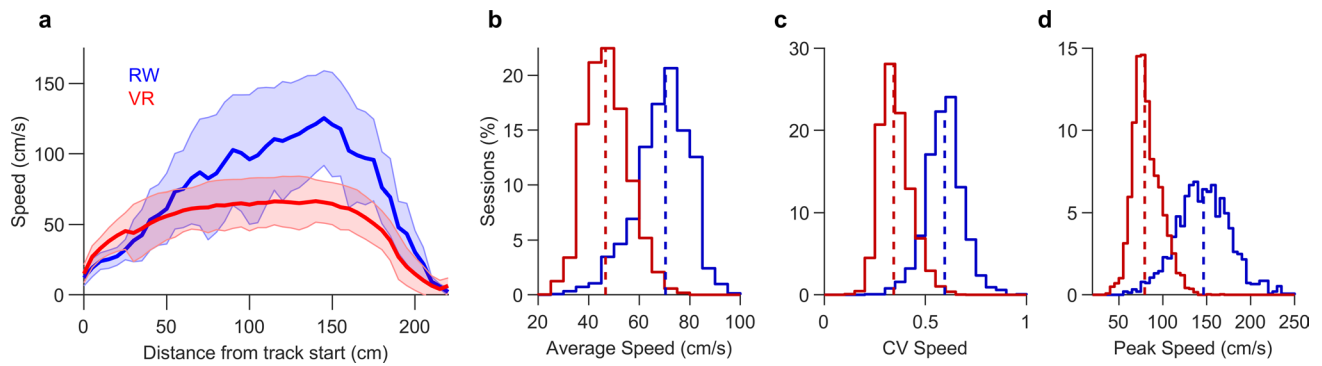
Extended Data Fig. 1 | Additional examples of -4 Hz eta oscillation during running in VR, but not in RW. The data were recorded from rat #1 and rat #2. Similar format as Fig. 1. **a–b, h–i**, Traces of LFP, raw (grey), filtered in theta (6–10 Hz, cyan) and eta (2.5–5.5 Hz, magenta) bands during high-speed (above 15 cm/s) running on track (top, i) and at low-speeds (below 15 cm/s) (bottom, ii) recorded on the same tetrodes in the same day RW (**a, h**) and VR (**b, i**). **c, j**, Amplitude envelope distribution during high- (30–60 cm/s) and low- (5–15 cm/s) speed runs for the theta (left panel) and eta (right panel) bands in RW. Theta amplitude was significantly (rat #1, $p < 10^{-10}$, $X^2 = 822.14$; rat #2, $p < 10^{-10}$, $X^2 = 218.0$, KW test) larger at high speeds than low speeds, whereas eta amplitude was slightly smaller at high speeds (rat #1, $p = 10^{-10}$, $X^2 = 49.5$; rat #2, $p < 10^{-10}$, $X^2 = 359.5$, KW test). **d, k**, Similar to **c**, but for VR showing large and significant increase in both eta (rat #1, $p < 10^{-10}$, $X^2 = 7942.7$; rat #2, $p < 10^{-10}$, $X^2 = 279.76$, KW test) and theta (rat #1, $p < 10^{-10}$, $X^2 = 5542.9$; rat #2, $p < 10^{-10}$, $X^2 = 259.14$, KW test) amplitudes at higher speeds. **e, f, l, m**, Power spectra of the example LFPs in RW (blue) and VR (red) during running (**e, l**) and immobility (**f, m**). **g, n**, Power index, during run compared to stop, showing prominent peaks in both eta and theta bands in VR (red) and only in theta band in RW (blue). (***) $p < 10^{-10}$.



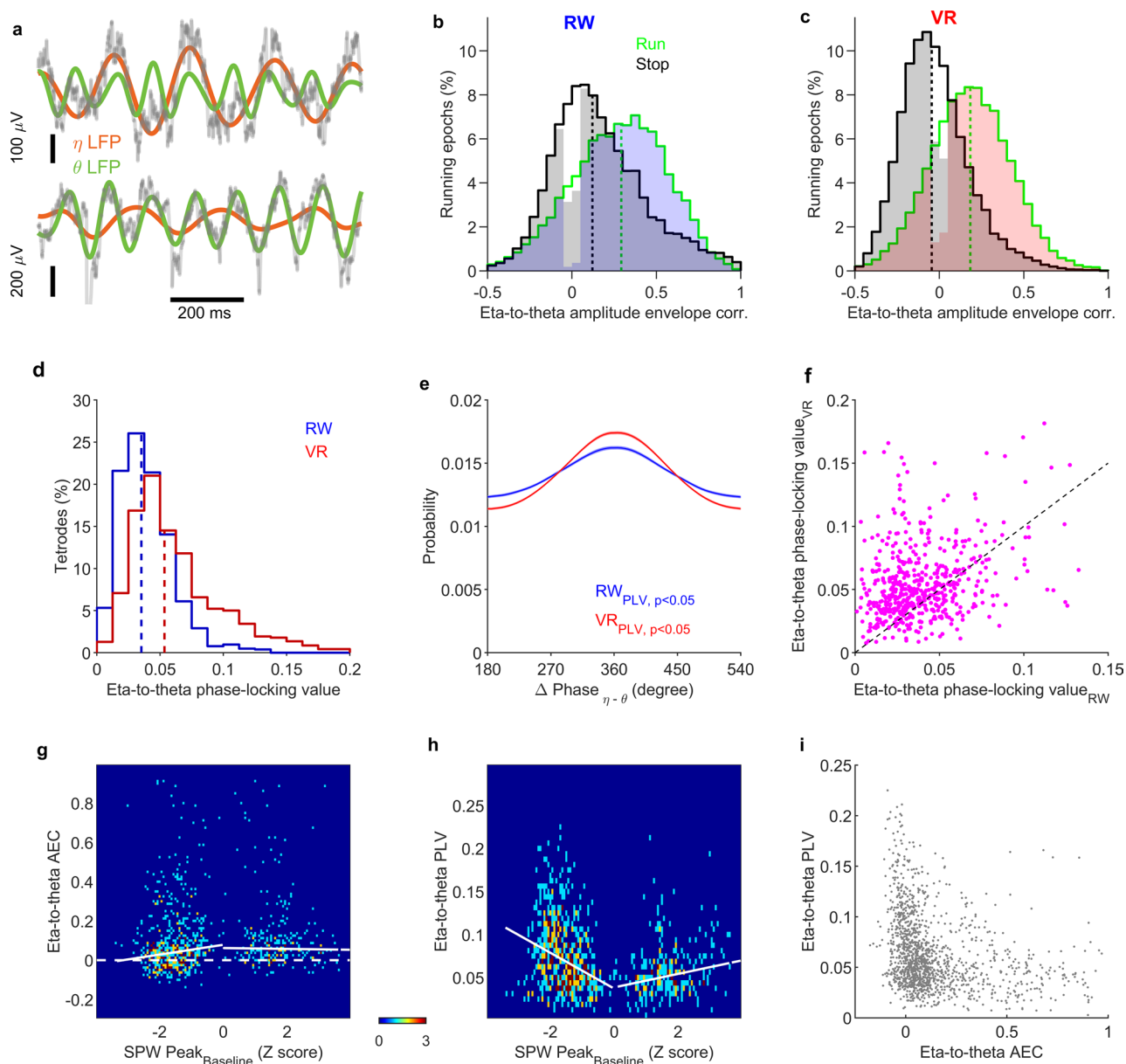
Extended Data Fig. 2 | Additional examples of ~4 Hz eta oscillation during running in VR. The data were recorded from rat #5, rat #6 and rat #7. Similar format as Fig. 1. **a, b**, Left, Traces of LFP, raw (grey), filtered in theta (6–10 Hz, green) and eta (2.5–5.5 Hz, brown) bands during high-speed (above 15 cm/s) running on track (top) and at low-speeds (below 15 cm/s) (bottom) recorded in the VR. Middle, (bottom panel) Power spectra of the example LFPs in VR during running (red) and immobility (black), and (top panel) power index, during run compared to stop, showing prominent peaks in both eta and theta bands in VR (red). Right, Amplitude envelope distribution during high- (30–60 cm/s) and low- (5–15 cm/s) speed runs for the theta (top panel) and eta (bottom panel) bands in VR. Theta amplitude was significantly (rat #5, $p < 10^{-10}$, $X^2 = 1430.5$; rat #6, $p < 10^{-10}$, $X^2 = 4357.1$; rat #7, $p < 10^{-10}$, $X^2 = 2661.0$, KW test) larger at high speeds than low speeds, whereas eta amplitude was slightly smaller at high speeds (rat #5, $p < 10^{-10}$, $X^2 = 3434.0$; rat #6, $p < 10^{-10}$, $X^2 = 12250.0$; rat #7, $p < 10^{-10}$, $X^2 = 1997.3$, KW test).



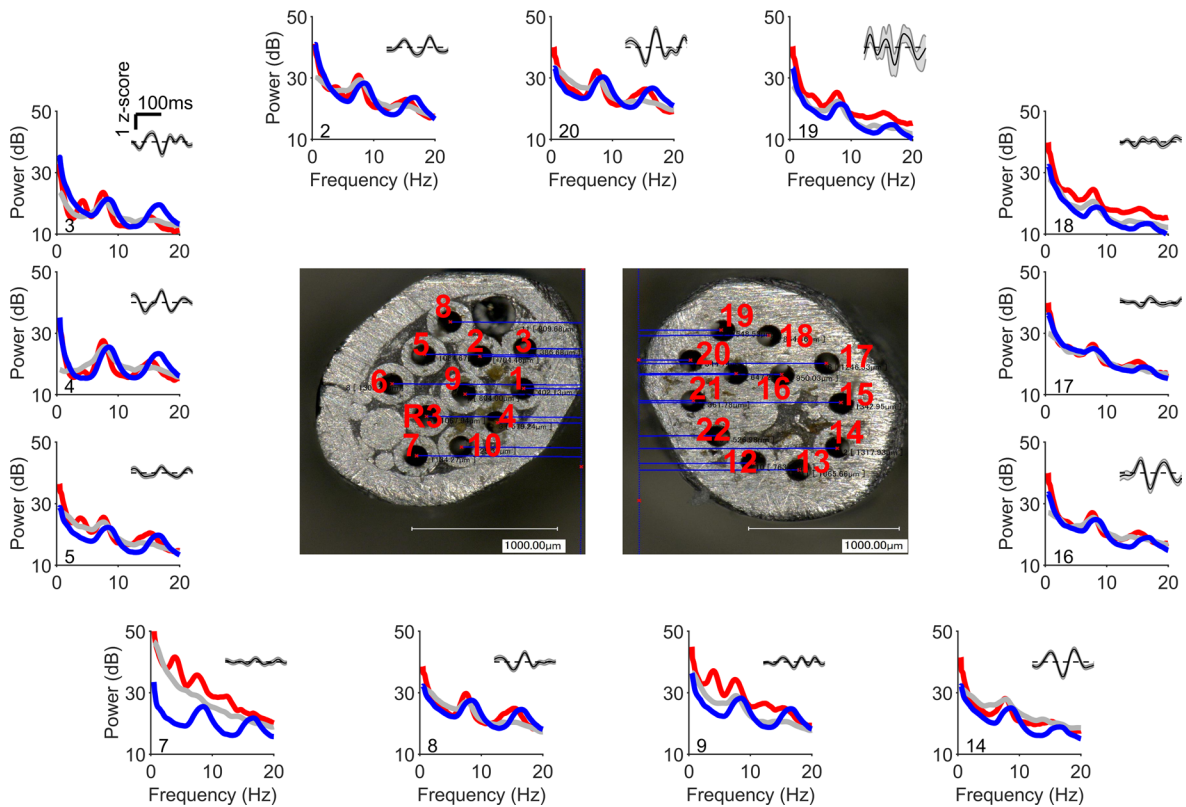
Extended Data Fig. 3 | Differential effect of speed on eta amplitude and theta frequency in RW and VR. **a**, Running speed of the rat (top, black) and the corresponding LFP (same format as in Fig. 1a) in VR. Both theta and eta amplitudes increase with speed. **b**, Same tetrode measured in RW on the same day showing speed-dependent increase in theta, but not eta, amplitude. **c,d**, Individual LFP eta-cycle amplitude and corresponding speed in VR (**c**) and RW (**d**) for the entire session in **a** and **b**. The broken axis separates two speed ranges - below (outlined) and above 10 cm/s. Each small dot indicates one measurement. The square dots show mean and s.e.m. in each bin in RW (blue) and VR (red). A log speed scale was used for the speed range below 10 cm/s. Linear regression fits are shown separately for both speed ranges (black lines). **e**, Population averaged theta amplitude, showing strong increase with running speed in RW. Population averaged theta amplitude in VR first decreased at low speeds (0 vs 10 cm/s) and then increased comparable to RW (Supplementary Table 1). **f**, Same as 3e, but for theta frequency showed significant increase with running speed in RW, but in VR the frequency dropped at very low speeds (0 vs 10 cm/s), and then became speed-independent. **g**, Same as 3e, but for eta amplitude, showing decrease in eta amplitude with increasing running speed for RW, but sharp drop in eta amplitude at low speeds (0 vs 10 cm/s), and steady increase in amplitude at higher speeds in VR. **h**, Same as 3e, but for eta frequency, showing no clear dependence of eta frequency on running speed in both RW and VR. **i**, Individual eta-cycle amplitudes are positively correlated with speed above 10 cm/s across tetrodes in VR (0.09 ± 0.001 , $p < 10^{-10}$), but not in RW (-0.107 ± 0.005 , $p < 10^{-10}$). 7.5% and 43.1% of all tetrode showed significant increase in eta amplitude with running speed in RW and VR, respectively ($p < 0.05$). **j**, Individual eta-cycle amplitudes are negatively correlated with speed below 10 cm/s across tetrodes in VR (-0.095 ± 0.003 , $p < 10^{-10}$), but not in RW (0.002 ± 0.003 , $p = 0.1$). Shaded areas and error bars denote s.e.m.



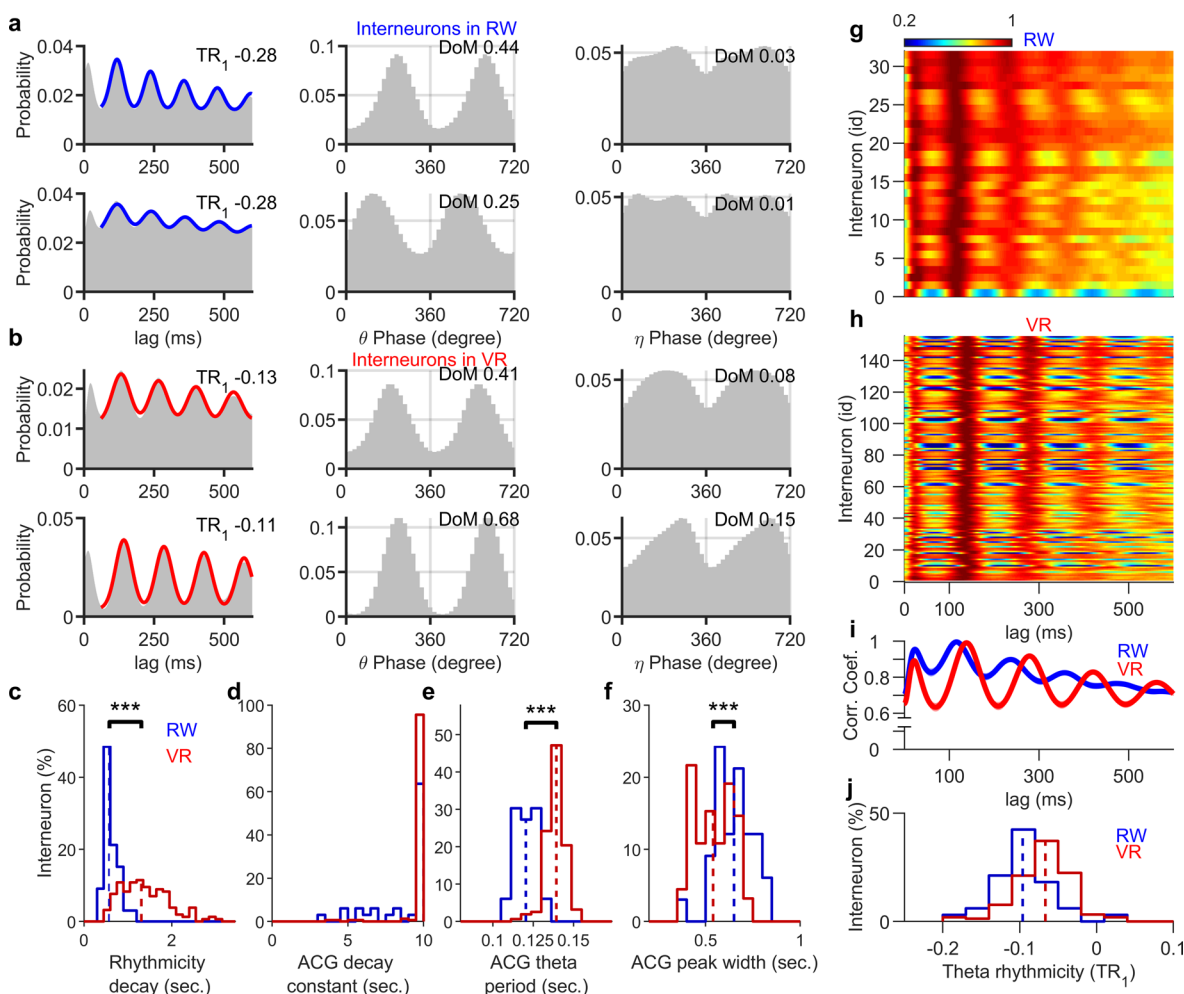
Extended Data Fig. 4 | Running speed in the linear track in RW and VR. **a**, Running speed (means \pm SD) of the rats as a function of position on a 2.2-m-long linear track for RW (blue) and VR (red). Although the rats were faster in RW, their behavior was similar, reliably reducing speed before reaching the end of the track ($n = 49$ sessions in RW, $n = 121$ sessions in VR). **b**, Average speeds in RW (69.42 ± 0.27) were significantly greater ($p < 10^{-10}$, $\chi^2 = 2502.3$, KW test) than in VR (47.00 ± 0.15). **c**, CV of running speeds in RW (0.59 ± 0.0023) were significantly greater ($p < 10^{-10}$, $\chi^2 = 2933.6$, KW test) than in VR (0.35 ± 0.0012). **d**, Average speeds in RW (147.13 ± 0.02) were significantly greater ($p < 10^{-10}$, $\chi^2 = 2872.7$, KW test) than in VR (81.48 ± 0.0046). Shaded areas in **a** denote s.e.m.



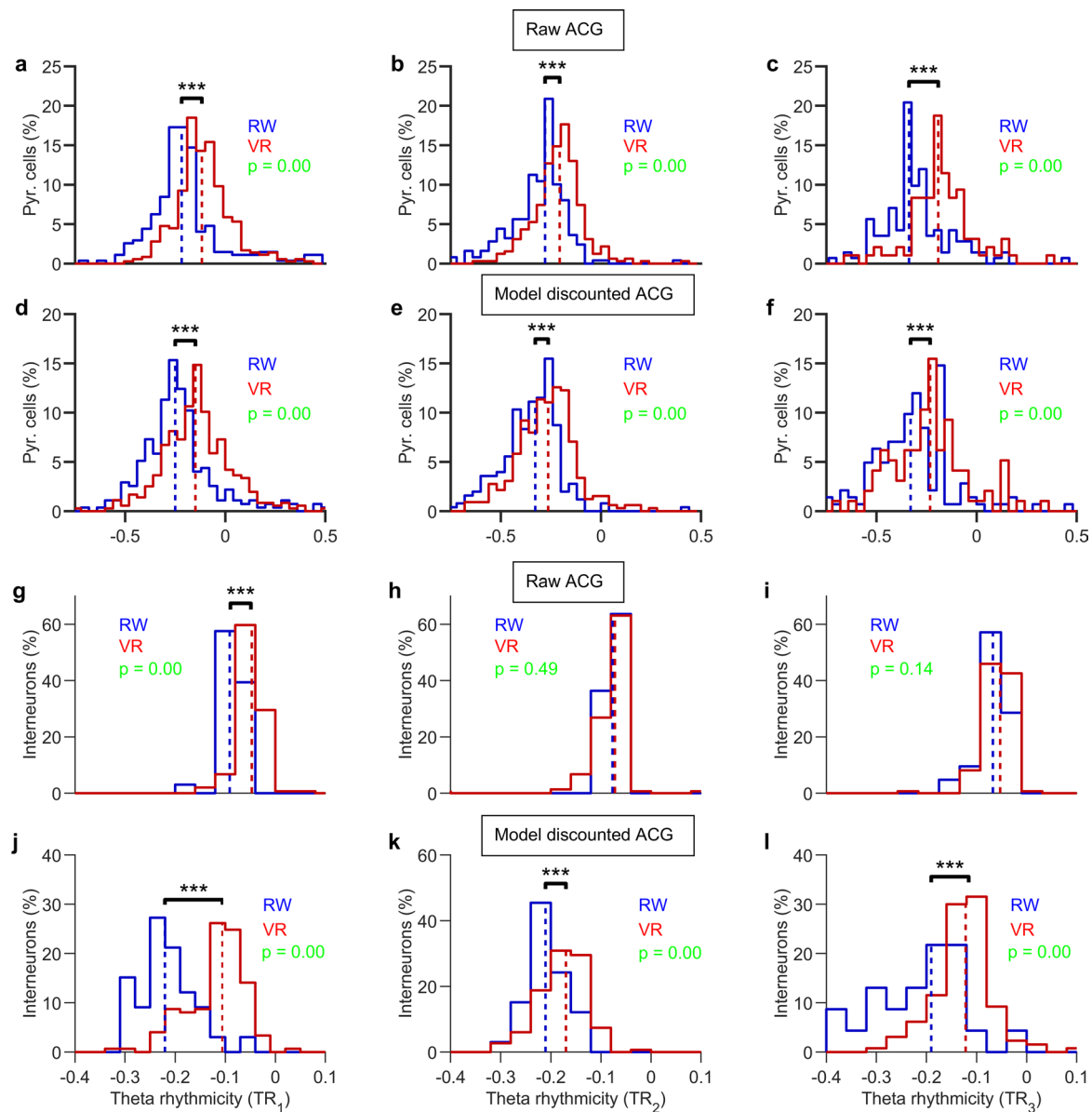
Extended Data Fig. 5 | Eta-theta phase-phase coupling but not eta-theta amplitude- amplitude coupling is far greater in VR than in RW during running. **a**, Example traces showing co-existence of eta and theta. Traces of LFP, raw (grey), filtered in theta (6–10 Hz, green) and eta (2.5–5.5 Hz, brown) bands are shown during high-speed (above 15 cm/s) running on track. **b**, Distributions of the eta-theta amplitude envelope correlation (AEC) during running (>5 cm/s, 0.27 ± 0.0019) and stops at goal location (0.16 ± 0.0017) in RW were significantly different ($p < 10^{-10}$, $X^2 = 2178.2$, KW test). Shaded area indicates significant correlations. **c**, Same as in b, but in VR. Distributions of theta-to-eta amplitude envelope correlation (AEC) during runs in track (>5 cm/s, 0.18 ± 0.0013) and stops at goal location (-0.02 ± 0.0011) in VR were significantly different ($p < 10^{-10}$, $X^2 = 2499.4$, KW test). **d**, Phase locking values (PLV) were computed as the mean vector length of the differences between instantaneous LFP theta and eta phases (See methods). The distribution of the LFP eta-to-theta PLV across the tetropdes was significantly smaller ($p < 10^{-10}$, $X^2 = 331.56$, KW test) in RW (0.039 ± 0.0006) than in VR (0.063 ± 0.0017). **e**, Distributions of eta-to-theta phase differences in RW (blue) and VR (red) for tetropdes with significant PLV. **f**, Eta-to-theta PLV for the same tetropdes in RW versus in VR recorded in the same day sessions, showed that 72% of tetropdes had greater eta-theta PLV in VR than RW. **g, h**, Relationship between SPW amplitude and polarity and **(g)** eta-to-theta amplitude envelope correlation (AEC) (for positive SPW $n = 279$, $r = -0.05$, $p = 0.397$, for negative SPW, $n = 617$, $r = 0.155$, $p < 10^{-5}$), and **(h)** phase locking value (PLV) (for positive SPW $n = 279$, $r = 0.18$, $p = 0.005$, for negative SPW, $n = 617$, $r = -0.3128$, $p < 10^{-10}$) in VR. Eta-theta phase-phase coupling is larger for tetropdes with larger magnitude SPW, for both +ve and -ve polarity SPW. The picture is reversed for the AEC. Number indicates max value. **i**, Scatter plot between eta-to-theta AEC and PLV in VR ($r = -0.343$, $p < 10^{-10}$).



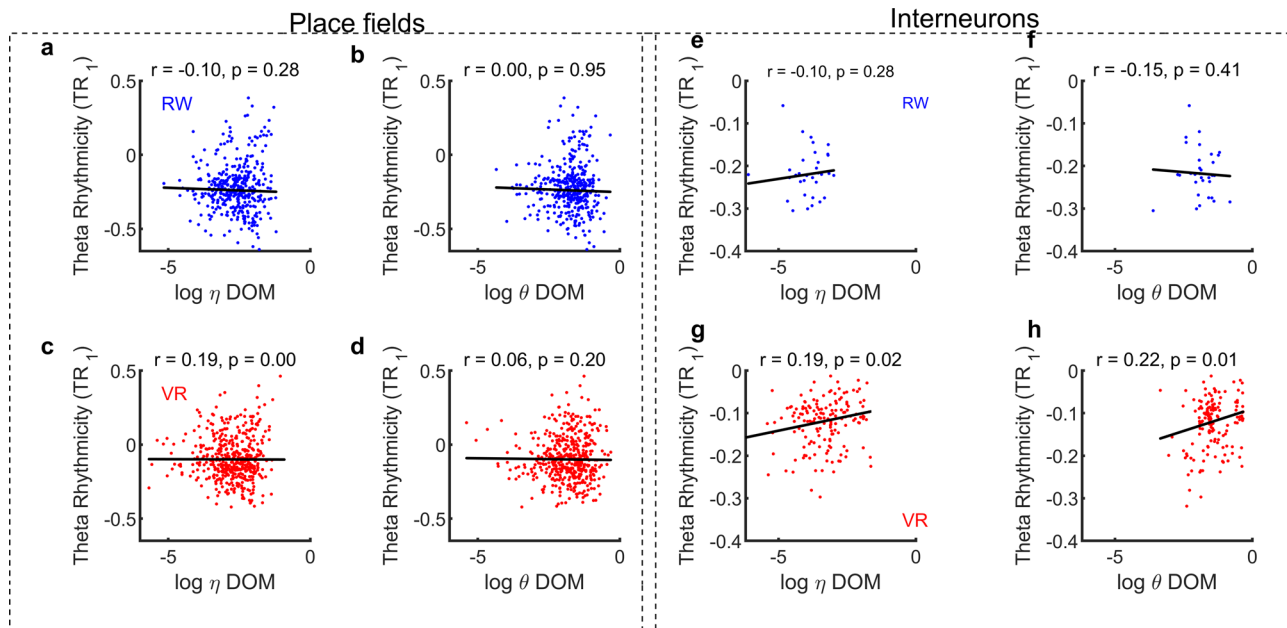
Extended Data Fig. 6 | Prominent eta band peak appears only during running in VR on tetrodes with small SPW, independent of the planer position of the electrodes. LFP power spectra for simultaneously recorded tetrodes are shown during running (red) and immobility (grey) in VR. Power spectra of the same tetrodes during running in RW are also shown (blue). Average z-scored sharp-waves computed from the baseline session preceding the VR session are shown for each tetrode (grey inset). Tetrode numbers are shown at left bottom corner of the power spectra. **Center:** Pictures of the bilateral cannulae with tetrode numbers (red). These are not sequential here because the numbers are determined by their sequential position in the electrode interface board.



Extended Data Fig. 7 | Model fit of autocorrelograms of interneurons in RW and VR. (a, b) Examples of interneurons' autocorrelograms (grey) with TR_1 values are shown along with fits using GMM in RW (a, top two rows, left, blue) and in VR (b, bottom two rows, left, red). The distribution of spikes' theta (middle column) and eta (right column) phases are given. (c) Histograms of ACG rhythmicity decay in RW (blue, $n=36$, 0.64 ± 0.04) and VR (red, $n=157$, 1.4 ± 0.04) are significantly different ($p < 10^{-10}$, $\chi^2 = 81.37$). (d) Histograms of ACG decay constant in RW (blue, 8.4 ± 0.39) and VR (red, 9.8 ± 0.07) are shown ($p < 10^{-5}$, $\chi^2 = 19.65$). (e) Histograms of ACG theta period in RW (0.12 ± 0.015) and VR (0.138 ± 0.02) are significantly different ($p < 10^{-10}$, $\chi^2 = 82.63$). (f) Histograms of ACG peak widths in RW (0.65 ± 0.002) and VR (0.54 ± 0.0012) are significantly different ($p = 1.1 \times 10^{-7}$, $\chi^2 = 23.71$). (g, h) Heat map of ACGs of spike trains sorted by increasing TR_1 for putative interneurons recorded during running in RW (g) and VR (h). The ACGs are normalized by their first theta peak values. (i) The population average of autocorrelations shows greater theta rhythmicity in VR than in RW. (j) The histograms of the TR_1 distributions show significant difference between RW (median = -0.09) and VR (median = -0.07) ($p < 10^{-10}$, $\chi^2 = 57.02$).



Extended Data Fig. 8 | Theta rhythmicity index of the putative pyramidal cells and interneurons in RW and VR. **a-f** Data from putative pyramidal cells. **a**, TR_1 distributions in VR (-0.1 ± 0.0075 , $n = 355$) is much greater ($p < 10^{-10}$, $\chi^2 = 72.83$) than RW (-0.17 ± 0.014 , $n = 268$) and **b**, Difference of third-to-second peak of theta (TR_2) in VR (-0.21 ± 0.007 , $n = 153$) is much greater ($p < 10^{-10}$, $\chi^2 = 51.83$) than RW (-0.32 ± 0.0081 , $n = 186$). **c**, Difference of fourth-to-third theta peak (TR_3) in VR (-0.21 ± 0.008 , $n = 201$) is much greater ($p < 10^{-9}$, $\chi^2 = 33.58$) than in RW (-0.36 ± 0.013 , $n = 114$) and **d**, Same as **a**, but model corrected ACG estimates show TR_1 in VR (-0.14 ± 0.0091 , $n = 357$) is much greater ($p < 10^{-10}$, $\chi^2 = 54.44$) than in RW (-0.21 ± 0.014 , $n = 274$) and **e**, Difference of third-to-second peak (TR_2) difference index ($p = 2.5188e-05$, $\chi^2 = 17.75$) between RW (-0.32 ± 0.0153 , $n = 252$) and VR (-0.276 ± 0.009 , $n = 155$). **f**, Difference of fourth-to-third peak (TR_3) difference index ($p = 0.002$, $\chi^2 = 9.58$) between RW (-0.35 ± 0.014 , $n = 142$) and VR (-0.27 ± 0.009 , $n = 76$). **g-l** Similar to **a-d** but for interneurons. **g**, Significant difference of TR_1 distributions ($p < 10^{-10}$, $\chi^2 = 47.56$) cells between RW (-0.09 ± 0.004 , $n = 33$) and VR (-0.05 ± 0.0033 , $n = 149$). **h**, Difference of third-to-second peak (TR_2) difference index ($p = 0.49$, $\chi^2 = 0.47$) between RW (-0.0767 ± 0.0031 , $n = 33$) and VR (-0.078 ± 0.0035 , $n = 149$). **i**, Difference of fourth-to-third peak (TR_3) difference index ($p = 0.13$, $\chi^2 = 2.18$) between RW (-0.066 ± 0.006 , $n = 33$) and VR (-0.05 ± 0.007 , $n = 148$). **j**, Significant difference of TR_1 distributions ($p = 4.8071e-12$, $\chi^2 = 47.76$) of putative pyramidal cells between RW (-0.215 ± 0.0097 , $n = 33$) and VR (-0.116 ± 0.0048 , $n = 149$). **k**, Difference of third-to-second peak (TR_2) difference index ($p < 10^{-5}$, $\chi^2 = 16.29$) between RW (-0.21 ± 0.0075 , $n = 33$) and VR (-0.153 ± 0.0098 , $n = 149$). **l**, Difference of fourth-to-third peak (TR_3) difference index ($p = 2.3933e-06$, $\chi^2 = 22.25$) between RW (-0.21 ± 0.0187 , $n = 23$) and VR (-0.115 ± 0.0076 , $n = 130$). (***, $P < 0.001$).



Extended Data Fig. 9 | Relationship between theta rhythmicity and theta and eta phase locking of place cells and interneurons in RW and VR. (a, b) We quantified the relationship between TR_{-1} and eta ($r = -0.1, p = 0.28$, partial Pearson correlation with number of spikes as controlling variable) and theta ($r = 0.0032, p = 0.95$) phase locking of place cells in RW. **(c, d)** The place cells with higher TR_{-1} showed increasingly more eta ($r = 0.22, p < 10^{-5}$), but not theta ($r = 0.06, p = 0.2$), phase locking in VR. **(e, f)** No systematic relationship was found between TR_{-1} and **(e)** eta ($r = -0.1, p = 0.28$) or **(f)** theta ($r = -0.15, p = 0.41$) phase locking in RW for interneurons. **(g, h)** Instead, interneurons with higher TR_{-1} showed increasingly more **(g)** eta ($r = 0.19, p = 0.02$) and **(h)** theta ($r = 0.22, p = 0.01$) phase locking in VR.

Reporting Summary

Nature Research wishes to improve the reproducibility of the work that we publish. This form provides structure for consistency and transparency in reporting. For further information on Nature Research policies, see our [Editorial Policies](#) and the [Editorial Policy Checklist](#).

Statistics

For all statistical analyses, confirm that the following items are present in the figure legend, table legend, main text, or Methods section.

- | | |
|-----|-----------|
| n/a | Confirmed |
|-----|-----------|
- The exact sample size (n) for each experimental group/condition, given as a discrete number and unit of measurement
 - A statement on whether measurements were taken from distinct samples or whether the same sample was measured repeatedly
 - The statistical test(s) used AND whether they are one- or two-sided
Only common tests should be described solely by name; describe more complex techniques in the Methods section.
 - A description of all covariates tested
 - A description of any assumptions or corrections, such as tests of normality and adjustment for multiple comparisons
 - A full description of the statistical parameters including central tendency (e.g. means) or other basic estimates (e.g. regression coefficient) AND variation (e.g. standard deviation) or associated estimates of uncertainty (e.g. confidence intervals)
 - For null hypothesis testing, the test statistic (e.g. F , t , r) with confidence intervals, effect sizes, degrees of freedom and P value noted
Give P values as exact values whenever suitable.
 - For Bayesian analysis, information on the choice of priors and Markov chain Monte Carlo settings
 - For hierarchical and complex designs, identification of the appropriate level for tests and full reporting of outcomes
 - Estimates of effect sizes (e.g. Cohen's d , Pearson's r), indicating how they were calculated

Our web collection on [statistics for biologists](#) contains articles on many of the points above.

Software and code

Policy information about [availability of computer code](#)

Data collection

Data analysis

For manuscripts utilizing custom algorithms or software that are central to the research but not yet described in published literature, software must be made available to editors and reviewers. We strongly encourage code deposition in a community repository (e.g. GitHub). See the Nature Research [guidelines for submitting code & software](#) for further information.

Data

Policy information about [availability of data](#)

All manuscripts must include a [data availability statement](#). This statement should provide the following information, where applicable:

- Accession codes, unique identifiers, or web links for publicly available datasets
- A list of figures that have associated raw data
- A description of any restrictions on data availability

Field-specific reporting

Please select the one below that is the best fit for your research. If you are not sure, read the appropriate sections before making your selection.

Life sciences Behavioural & social sciences Ecological, evolutionary & environmental sciences

For a reference copy of the document with all sections, see [nature.com/documents/nr-reporting-summary-flat.pdf](https://www.nature.com/documents/nr-reporting-summary-flat.pdf)

Life sciences study design

All studies must disclose on these points even when the disclosure is negative.

Sample size	No statistical methods were used to pre-determine sample size in these exploratory studies, but our sample sizes are similar to those reported in previous publications.
Data exclusions	No rat was excluded. The presence of the sharp wave ripples was used to identify hippocampal tetrodes. In addition, classified putative pyramidal cells were used to verify selection. Both methods were widely used to verify hippocampal tetrodes.
Replication	The results were replicated in seven different rats. Moreover, preliminary study showed the main effect across different VR tasks, when different rats were used. The robust main effects were found in all 7 animals and replicated successfully across all subjects.
Randomization	Similar sessions in real world and virtual reality were run overall rats, which were selected randomly. Covariates were controlled across sessions and within rats.
Blinding	Neural and behavioral data analyses were conducted in an identical way regardless of the identity of the experimental condition from which the data were collected, with the investigator blinded to group allocation during data collection and/or analysis. Hippocampal units were isolated and cluster by three different lab members blindly. The experiments were conducted by three different lab members.

Reporting for specific materials, systems and methods

We require information from authors about some types of materials, experimental systems and methods used in many studies. Here, indicate whether each material, system or method listed is relevant to your study. If you are not sure if a list item applies to your research, read the appropriate section before selecting a response.

Materials & experimental systems

n/a	Included in the study
<input checked="" type="checkbox"/>	<input type="checkbox"/> Antibodies
<input checked="" type="checkbox"/>	<input type="checkbox"/> Eukaryotic cell lines
<input checked="" type="checkbox"/>	<input type="checkbox"/> Palaeontology and archaeology
<input type="checkbox"/>	<input checked="" type="checkbox"/> Animals and other organisms
<input checked="" type="checkbox"/>	<input type="checkbox"/> Human research participants
<input checked="" type="checkbox"/>	<input type="checkbox"/> Clinical data
<input checked="" type="checkbox"/>	<input type="checkbox"/> Dual use research of concern

Methods

n/a	Included in the study
<input checked="" type="checkbox"/>	<input type="checkbox"/> ChIP-seq
<input checked="" type="checkbox"/>	<input type="checkbox"/> Flow cytometry
<input checked="" type="checkbox"/>	<input type="checkbox"/> MRI-based neuroimaging

Animals and other organisms

Policy information about [studies involving animals](#); [ARRIVE guidelines](#) recommended for reporting animal research

Laboratory animals	Seven, adult, male, Long-Evans rats (approximately 3.5 months old at the start of training) were used in this study.
Wild animals	Wild animals were not used in this study.
Field-collected samples	No field collected samples were used in the study.
Ethics oversight	All experimental procedures were approved by the UCLA Chancellor's Animal Research Committee and were conducted in accordance with USA federal guidelines.

Note that full information on the approval of the study protocol must also be provided in the manuscript.